# Numerical study of the hydrodynamic drag force in atomic force microscopy measurements undertaken in fluids

J.V. Mendez-Mendez[a,b,*], M.T. Alonso-Rasgado[b], E. Correia Faria[c], E.A. Flores-Johnson[d], R.D. Snook[c]

[a]Centro de Nanociencias y Micro-Nanotecnología del IPN, Unidad Profesional Adolfo López Mateos, Calle Luis Enrique Erro s/n, Col. Zacatenco, C.P. 07738, México D.F., Mexico.

[b]School of Mechanical, Aerospace and Civil Engineering, The University of Manchester, Manchester M60 1QD, UK.

[c]Manchester Institute of Biotechnology, School of Chemical Engineering and Analytical Science, The University of Manchester, Manchester M1 7DN, UK.

[d]School of Civil Engineering, The University of Sydney, Sydney, NSW 2006, Australia.

**Abstract**: When atomic force microscopy (AFM) is employed for in vivo study of immersed biological samples, the fluid medium presents additional complexities, not least of which is the hydrodynamic drag force due to viscous friction of the cantilever with the liquid. This force should be considered when interpreting experimental results and any calculated material properties. In this paper, a numerical model is presented to study the influence of the drag force on experimental data obtained from AFM measurements using computational fluid dynamics (CFD) simulation. The model provides quantification of the drag force in AFM measurements of soft specimens in fluids.

The numerical predictions were compared with experimental data obtained using AFM with a V-shaped cantilever fitted with a pyramidal tip. Tip velocities ranging from 1.05 to 105 µm/s were employed in water, polyethylene glycol and glycerol with the platform approaching from a distance of 6000 nm. The model was also compared with an existing analytical model. Good agreement was observed between numerical results, experiments and analytical predictions. Accurate predictions were obtained without the need for extrapolation of experimental data. In addition, the model can be employed over the range of tip geometries and velocities typically utilized in AFM measurements.

[*]Corresponding author. Tel.: +52 55 57296000 Ext. 57506, Fax: +52 55 2729 6000 Ext 46080, Email: jmendezm@ipn.mx

## 1. Introduction

Atomic Force Microscopy (AFM) is finding increasing use in biological applications as a tool for investigating the mechanical properties of cells and forces between molecules, in addition to providing 3D surface profiles with high resolution [1-3]. One of the major advantages of AFM is the ability to undertake measurements of specimens in fluid environments. This advantage is particularly valuable because it allows undertaking investigations of

biological samples in their natural, physiological environment [4-12].

The AFM force measurements on soft samples in fluid environments are affected by a hydrodynamic drag force, which results from the viscous friction of the cantilever with the surrounding fluid. This effect appears more significant when cantilever-tip velocities are above a few µm/s [4, 13-15]. Under such circumstances, the drag force is dependent upon factors including the stiffness, dimensions and velocity of the cantilever, the fluid viscosity, and the cantilever/tip-surface separation [4, 13]. AFM cantilever dynamics in liquids remains little understood and requires further investigations [16, 17]. In cases where the magnitudes of the measured forces are low, e.g. when determining the elastic properties of soft materials such as biological cells, then the drag force can be of a similar order to the reaction force of the sample [13]. Under such circumstances, significant errors in measurement can occur if the hydrodynamic drag force is not accounted for. This usually limits the cantilever velocities to below 10 µm/s [13]. While hydrodynamic forces have been calculated for certain geometries such as spheres moving through viscous fluids [18, 19] as they approach a surface at low Reynolds number, it is not possible to directly assess the drag forces on the cantilever-tip arrangement of the AFM during the probing of soft samples in liquid environments as there is no means of accurately determining the force generated by the sample [4].

Researchers have utilized a variety of means in an attempt to account for the drag force in AFM measurements. Ma et al. [20] investigated the zero frequency hydrodynamic drag coefficient of a tipless V-shaped AFM cantilever in distilled water at different separations of the cantilever with respect to a glass surface, and they found that the experimental data obtained, which demonstrates the increase in drag coefficient as the probe approaches the surface, could be well represented by Brenner's model [18] for a sphere moving normally towards a rigid surface. This observation suggests that there is an inverse scaling relationship between hydrodynamic drag force and cantilever-surface separation.

An investigation of the effects of hydrodynamic drag on AFM measurements of soft samples using rectangular and V-shaped cantilevers in liquids at low Reynolds numbers was undertaken by Alcaraz et al. [4]. This research confirmed that the hydrodynamic drag force exhibits a locally pure viscous behavior and that the drag factor is dependent upon distance between the tip and the substrate. The authors pointed out that previous attempts to correct AFM measurements for hydrodynamic drag effects consisted of estimating the drag force at some distance above the specimen and then using this value to correct the measurements taken on contact [21-23]. However, it is expected that this approach will lead to an underestimation of the actual hydrodynamic drag at contact and the authors noted that applying corrective drag force measurements taken at even a few microns above the sample can lead to significant errors in the measured forces. In their findings, Alcaraz et al. suggested to use a scaled spherical model for the cantilever to more accurately account for the drag factor dependence on distance. In the model envisaged, the cantilever and tip arrangement is represented by a 1-D oscillator with an effective mass and spring constant. The force on the cantilever is considered to consist of two components: the force applied by the sample and the viscous drag force. The analysis leads to a scaled spherical model of the cantilever which enables the drag factor at contact to be estimated by extrapolating drag factor data

obtained in non-contact measurements obtained at various distances from the substrate. The model contains two empirical coefficients: the cantilever effective sphere radius and the effective tip height.

Janovjak et al. [13] investigated the hydrodynamic drag forces in single-molecule force measurements in AFM using the scaled spherical model proposed by Alcaraz et al [4]. The authors pointed out that hydrodynamic effects become particularly significant at pulling speeds greater than 10 µm/s, when they reach a similar order of magnitude to the molecular forces. Using this model, they quantified the hydrodynamic drag force as a function of pulling speed and tip-sample separation for two V-shaped AFM cantilevers and found that while drag force exhibited a linear dependence on pulling speed, the relationship with tip-surface separation was more complex in nature. In addition, the authors investigated the hydrodynamic effects during the unfolding of an individual molecule of a multi domain protein and they found that if hydrodynamic effects are considered then AFM force measurements can be more accurately evaluated at pulling speeds greater than a few µm/s.

The methods described above rely on extensive experiments to determine the coefficients to be used in the models. The aim of the work described in this paper is to develop a numerical model that enables the hydrodynamic drag forces present during AFM measurements of soft samples in fluids to be accurately quantified without the need to determine empirical coefficients or extrapolate data, and which is applicable for the range of tip geometries and velocities typically employed in AFM measurements. Motivation for the work stemmed from the need to reduce uncertainty in the interpretation of AFM data obtained from studies of soft samples in fluids, data that is

subsequently used to estimate the elastic properties of the specimens.

## 2. Materials and methods

Drag force measurements were carried out at room temperature in three fluids of different dynamic viscosities and densities, polyethylene glycol 300(285-315) g/mol (Sigma UK, Poole, UK), glycerol (Fisher Scientific UK Ltd, Loughborough, UK) and water on glass, mica and stainless steel substrates. Although polyethylene glycol and glycerol are not fluids used commonly in biology, these fluids were also used for easier visualization of the drag forces in both experimental and numerical results and to demonstrate the capabilities of the numerical model. A commercially available Picoforce Multimode AFM (Veeco, Cambridge, UK), which was equipped with a piezoelectric ceramic scanner enabling movement along the main X, Y and Z axes, was used. A silicon nitride V-shaped probe comprising a cantilever (Veeco DNP-20, 0.06 N/m nominal spring constant) with nominal dimensions of 196 µm length, 15 µm width and 0.6 µm thickness, and a 3 µm height silicon nitride pyramidal tip were employed for the tests. The determination of the spring constant of the probe was undertaken in fluid using the in-built Thermal Tune Method in air [24] prior to commencement of the experiments. Prior to using the Thermal Tune Method, the deflection sensitivity of the cantilever was obtained in liquid fluid by using the value of the inverse of the slope of the force curve while the cantilever was in contact with a hard glass surface. The average of the deflection sensitivity determined at 7 different points was 102.05 nm/V.

In the experimental tests, 30 µl of fluid were deposited on a piece of glass slice of dimension $5 \times 5$ mm$^2$. The glass slide was first cleaned by immersion in ethanol for 20

min follow by rinsing with distilled water. Measurements were carried out in each fluid in contact mode, with the cantilever moving at constant velocity from 6000 nm above the platform until the tip was brought into contact with the glass surface. Nine cantilever velocities, from the velocity range available (1.05-105 µm/s) for a 6000-nm displacement in the AFM, were employed: 1.05, 2.49, 4.02, 7.22, 13.1, 23.3, 29.9, 41.9 and 105 µm/s. The sampling frequency was 2048 points/cycle. Each experimental test was performed seven times in order to ensure repeatability of the results.

The viscosity of the polyethylene glycol and glycerol was determined using Bohlin C-VOR rheometer according with the manufacturer procedure by triplicated, and the properties of the water used were obtain in the literature.

# 3. Numerical simulations
## 3.1 Numerical model

The aim of the novel numerical model is to estimate the drag force during the motion of the cantilever of the AFM through the fluid towards the substrate and its subsequent retraction. Figure 1a shows the main components considered in the development of the numerical model including the cantilever, fluid medium, the glass slide, chip holder and cantilever chip. The model was developed using the commercially available ANSYS Workbench (Version 11.0) software. The fluid was modeled using the computational fluid dynamics (CFD) ANSYS CFX module, which was linked with the solid model of the cantilever modeled using the finite-element ANSYS Structural Mechanics module. The remaining components were modeled by the use of appropriate boundary conditions applied in the linked solid/fluid models.

The fluid flow model considered the fluid to be 3-D, single phase, viscous, incompressible and laminar in nature. A transient dynamic analysis (ANSYS flexible dynamic analysis) was undertaken for the cantilever. The overall simulation time for each analysis was calculated from the cantilever velocity and the distance travelled (6000 nm), giving simulation times between 5.71s (velocity = 1.05 µm/s) and 0.0571 s (velocity = 105 µm/s).

The ANSYS CFX model is based on the Reynolds averaged Navier-Stokes governing equations for incompressible fluids and can be written as the law of conservation of mass (Eq. (1)) and momentum equation for an incompressible turbulent fluid (Eq. (2)) [25]:

$$\frac{\partial U_i}{\partial x_i} = 0; \tag{1}$$

$$\frac{\partial U_i}{\partial t} + U_j \frac{\partial U_i}{\partial x_j} = -\frac{1}{\rho}\frac{\partial P}{\partial x_i} + \frac{\partial}{\partial x_j}\left(\nu \frac{\partial U_i}{\partial x_j} - \overline{u_i u_j}\right); \tag{2}$$

where $x_i$ represents the coordinate axes, $U_i$ is the mean velocity, $P$ is pressure, $\rho$ is the fluid density, $\nu$ viscosity of the medium and $\overline{u_i u_j}$ are the components of the Reynolds stress tensor [25]. The model used in our simulation is the laminar model governed by the unsteady Navier-Stokes equations. The correct selection of the model was verified by checking the output file, where the reference is that Re should be less than 1000 for laminar flow regime. The Re values found in our simulation were less than 1.

The fluid is shaped by the physical delimitation of the substrate (lower limit), the cantilever chip holder and the cantilever chip (upper limit) and the menisci formed due to the adhesion with the surroundings (see Figure 1a). The dimensions of the substrate are $5 \times 5$ mm$^2$ with a thickness of 1 mm. The cantilever chip holder shown in Figure 1b is made from glass and incorporates two fluid transfer ducts that enable continuous flow experiments to be performed if required (not used in the experiments described in this paper because both ducts were blocked).

**a ) Main components considered for the numerical model**



**b) Schematic of the cantilever chip holder with dimensions obtained from the manufacturer**

**c) Schematic of the cantilever chip with dimensions obtained from the manufacturer**



**d) Schematic of the cantilever Veeco DNP-20**
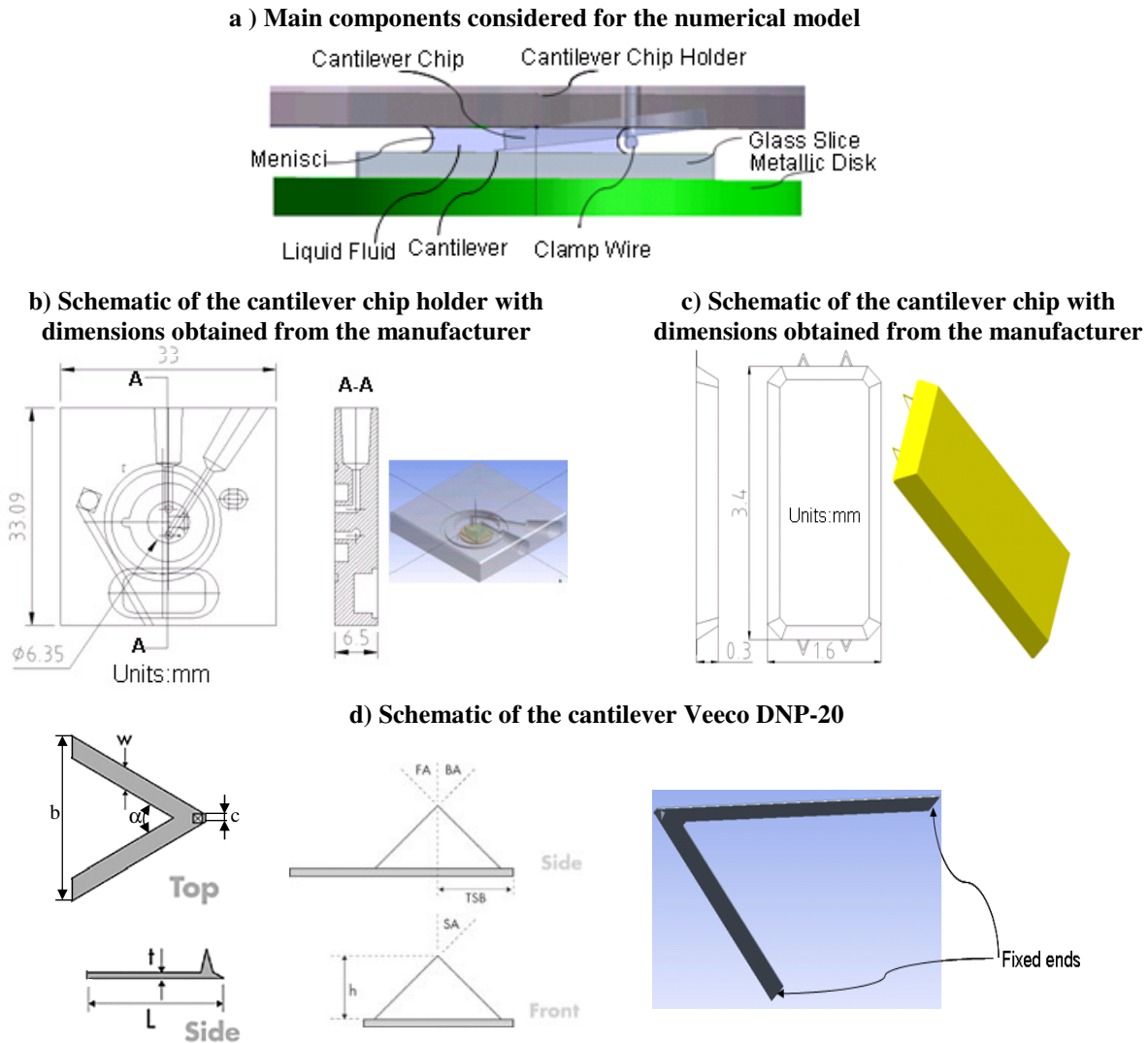


Figure 1. a) Main components considered for the numerical model, b) Schematic of the cantilever chip holder, c) Schematic of the cantilever chip, d) Schematic of the cantilever Veeco DNP-20.

The overall dimensions of the cantilever chip are shown in Figure 1c. A clamp wire is used to fix the cantilever chip to the cantilever chip holder (Figure 1a), however the detail of the wire is not included in the model because it is relatively remote from the area of interest. The fluid geometry is considered to be cylindrical in shape in the model.

The cantilever used in the experimental tests was a silicon nitride V-shaped (Veeco DNP-20) cantilever. The spring constant $k$ of the cantilever was 0.03544 N/m, which was determined using the Thermal Tune Method [24].

This method has an accuracy in the range of 6-15% [26]. The main cause for the error is that this method suffers from systematic errors in determining the correct deflection sensitivity [26]. Since there is a linear relationship between the elastic modulus $E$ of the cantilever and the spring constant $k$ (Section 3.2), and the value of $E$ used in the numerical model was calculated directly from $k$ (Section 3.2), this error is not included in the comparison of the experiments with the numerical results. Figure 1d and Table 1 give information concerning the cantilever and tip dimensions that were ascertained and subsequently utilized in the numerical model. Pictures taken using the camera attached to

the AFM were used to obtain the additional dimensions not provided by the manufacturer (Table 1).

Table 1. Dimensions used in the numerical model.

| Geometry | Value |
|---|---|
| Length $L$ (μm) | 196* |
| Thickness $T$ (μm) | 0.6* |
| Width $w$ (μm) | 15* |
| Tip height $h$ (μm) | 3* |
| Tip front, back and side angle $FA$, $BA$, $SA$ (°) | 35* |
| Front length $c$ (μm) | 4** |
| Distance between arms $b$ (μm) | 214** |
| Cantilever angle $\alpha$ (°) | 57.26*** |

* Provided by the manufacturer.
** Measured from micrographs.
***Calculated.

## 3.2 Cantilever

In the numerical model, it was considered that the cantilever was made of a single, homogeneous material. Adopting this assumption means that a methodology for calculating an effective value for the Young's modulus for the numerical model is therefore required.

A model of the V-shaped cantilever was created in ANSYS using the dimensions detailed in Figure 1d and Table 1. The resulting cantilever and tip model is shown in Fig. 1d. The cantilever was meshed with 5522 10-noded quadratic tetrahedral structural solid elements. The ends of the cantilever were fixed and a force was applied to the tip. The Young's modulus ($E$) was varied in the range 20-200 GPa. A deflection that was within the elastic range of the material and of a similar order of magnitude as that expected in the experimental tests was used (1.2 μm). For each of the values of Young's modulus considered, the cantilever model was run with the applied force being adjusted until the required deflection (1.2 μm) was obtained. From the resulting

deflections ($\delta$) and applied force ($F$), the cantilever stiffness $k$ was calculated using the Hooke's Law ($F = k \cdot \delta$).

By plotting $k$ versus $E$ (Fig. 2), the relationship $k = E(1.936 \times 10^{-7}$ m$)$ is obtained, which is linear as expected, since the model is based on the Euler-Bernoulli beam theory. Since the value of $k$ is known (Section 2.1), the corresponding effective Young's Modulus $E = 183.6$ GPa was obtained. This value is in close agreement with the value of $E = 173$ GPa obtained using Sader's analytical model [27]. The value of $E$ calculated using the finite element approach was used in our simulations because it is believed that this approach more accurately represents the cantilever geometry than any of the analytical models for the particular cantilever under consideration.

**Relationship between $k$ and $E$ for the V-shaped cantilever**
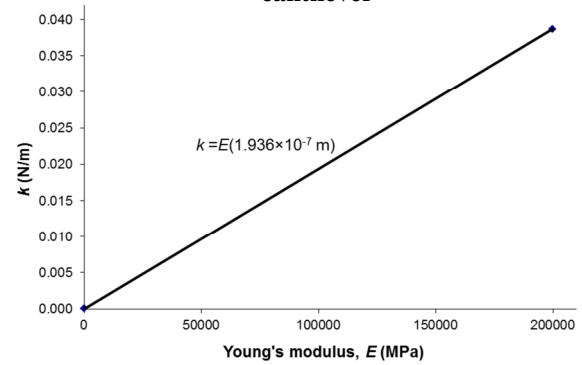


Figure 2. Relationship between $k$ and $E$ for the V-shaped cantilever.

## 3.3 Fluid model boundary conditions

The shape that the fluid medium takes in the AFM experimentation is shown in Figs. 3a and 3b. Based on this shape the following boundary conditions for the fluid model can be defined:

(i) *Surfaces open to atmosphere*: The menisci surfaces of the fluid are labeled 'open' in Fig. 3b. In the fluid model, these surfaces are considered to be subjected to atmospheric pressure, and it can move according with the base and top distance.

*(ii) No-slip boundary conditions*: The

portion of the fluid medium that contacts the substrate is marked 'base' in Fig. 3b. The surface denoted 'top' represents the top surface of the fluid in contact with the cantilever chip holder. The areas marked 'wallchip' and 'basechip' in Fig. 3a are the surfaces of the fluid that are in contact with walls and the base of the cantilever chip, respectively. On the 'base', 'top', 'wallchip' and 'basechip' surfaces, a no-slip boundary condition is applied (the fluid is considered to have zero velocity relative to the solid boundary).

*(iii) Specified displacement boundary conditions*: To simulate the motion of the cantilever through the fluid towards the substrate a specified displacement is applied to the 'base' surface. The displacement applied is calculated by giving the total distance travelled (6000 nm), the total number of time steps considered and the actual time step being analyzed.

*(iv) Cantilever model boundary conditions*: The cantilever model shown in Figure 1d was employed in the linked fluid/solid model of the cantilever and fluid medium. Fixed type boundary conditions (all degrees of freedom constrained) are applied on the surfaces marked 'fixed ends' in Fig. 1d; these surfaces represent the surfaces of the V-shaped cantilever that are bonded to the cantilever chip.

*(v) Cantilever-fluid contact boundary conditions*: A no slip boundary condition is applied on the cantilever surfaces in the model that are in contact with the fluid medium. The ANSYS Workbench (CFX) software automatically manages the coupling and linking of the cantilever and fluid medium models with force and deformation information being exchanged between the fluid and solid analysis modules during the solution process.

## 3.4 Meshes and time step

The 3D meshes of the fluid and cantilever are shown in Fig. 3c and Fig. 3d, respectively. The fluid geometry was meshed with a combination of tetrahedral, pyramidal and prism elements. The fluid mesh consisted of 462,581 4-noded linear tetrahedral elements, 3,700 5-noded linear pyramidal elements and 1,222 6-noded linear wedge (prism) elements. The cantilever was meshed with 5522 10-noded quadratic tetrahedral structural solid elements.

Thirty time steps were initially used in each simulation. In all cases, one complete cycle was simulated. The cycle/total simulation time ($t$) was calculated in each case from the velocity ($V$) and travelled cantilever distance ($d$) using $t = d/V$, where $d = 6000$ nm and $V = 1.05, 2.49, 4.02, 7.22, 13.1, 23.3, 29.9, 41.9$ and $105$ µm/s. This resulted in simulation times between 0.0571 s and 5.71 s and corresponding time step values ($\Delta t$) ranging from 0.0019 s to 0.19 s.

## 4. Results and discussion

Model predictions were compared with experimental results from the AFM tests and predictions of the empirical model of Alcaraz et al. [4], which was subsequently quantified by Janovjak et al. [13]. The experimental tests were designed to enable the investigation of the influence of tip velocity, tip-sample separation, fluid viscosity and substrate material on drag force and to provide experimental data for comparison with numerical predictions. The densities and dynamic viscosities of the fluids used in the experimental tests are given in Table 2; these properties were obtained using a Bohlin C-VOR rheometer and were required for the numerical model. The calculated Reynolds numbers for the experimental tests indicated that in all cases flow conditions were within the laminar regime.

**a) Top view of fluid medium shape in AFM experimentation showing the surfaces considered for the boundary conditions of the numerical model**
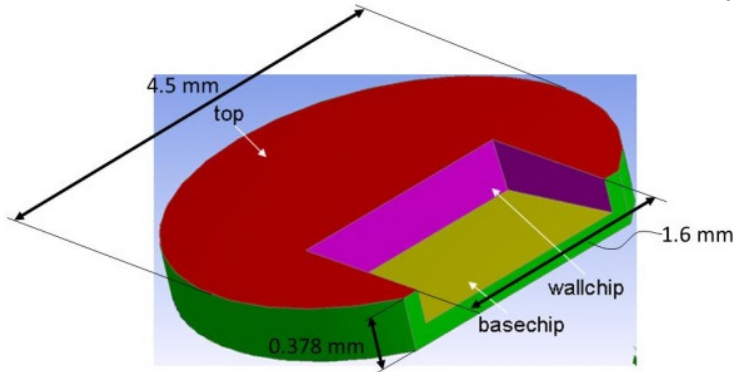
**b) Bottom view of fluid medium shape in AFM experimentation showing the surfaces considered for the boundary conditions of the numerical model**
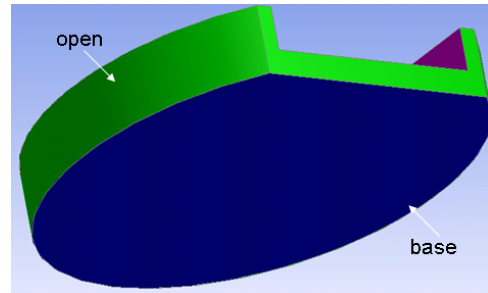
**c) 3D model mesh of the fluid**
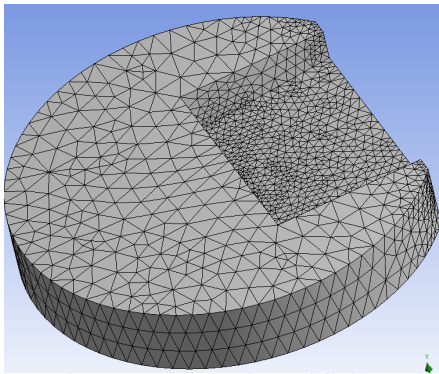
**d) 3D model mesh of the cantilever beam**
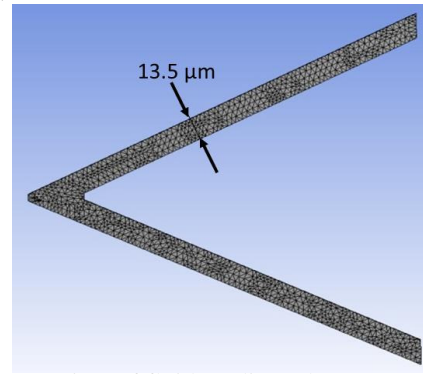
Figure 3. a) Top view of fluid medium shape, b) Bottom view of fluid medium shape, c) 3D model mesh of the fluid, d) 3D model mesh of the cantilever beam.

## 4.1 Methodology for determining drag force from experiments

To understand how drag force results were obtained from the force curves produced from the experimental tests, it is convenient to consider the approach curve from one of the tests undertaken. Figure 4a shows an approach curve, consisting of 1024 data points, obtained from an AFM experiment in water using a glass substrate with the platform moving towards the cantilever and tip at a constant velocity of 41.9 μm/s from an initial (vertical) distance of 6000 nm away. The point marked **A** in this figure denotes the start of the displacement, the point at which the platform begins to move towards the cantilever and tip. Point **B** indicates the cantilever-platform contact point. The analysis focuses on the zone between **A-B**, where the cantilever interacts only with the fluid and the substrate does not contribute to the force measured by the AFM.

Table 2. Properties at 20 ºC of fluids used in experimental tests.

| Material | Density (kg/m³) | Dynamic viscosity | SD |
|---|---|---|---|
| Water | 0.9982 | $1.002 \times 10^{-3}$ | - |
| Polyethylene Glycol (SIGMA) | 1.125 | 0.06902 | 0.024 |
| Glycerol (Fisher Scientific) | 1.259 | 0.9604 | 0.037 |

At point **A**, the cantilever tip-platform separation, *h,* is at its maximum and the drag force is zero. At point **B**, $h = 0$ and the drag force is at its maximum. The distance between these points is the total platform displacement, where no substrate interaction takes place.

8
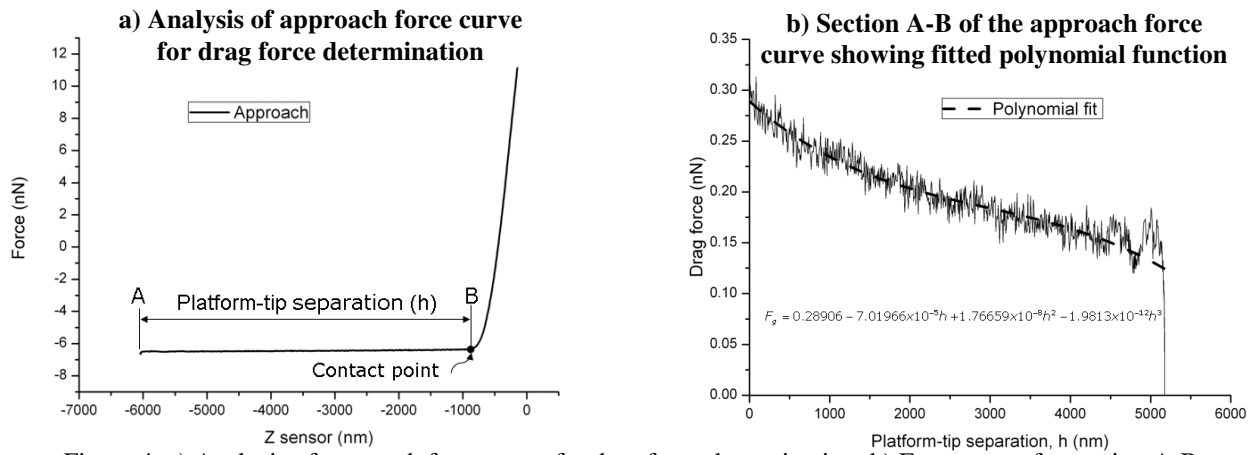
Figure 4. a) Analysis of approach force curve for drag force determination; b) Force curve for section A-B showing fitted polynomial function.

The section between points **A** and **B** in Fig. 4a is considered in more detail in Fig. 4b. It is noted that the X axis has been rearranged for clarity.

Between points **A** and **B** the cantilever interacts only with the fluid, therefore the force on the cantilever tip measured between these points is due only to this interaction, i.e., the hydrodynamic drag force. At the tip-platform contact point **B**, the platform has moved a distance 5167.542 nm from its initial position and the drag force has reached its maximum at approximately 0.3 nN.

To extract the hydrodynamic drag force data from the force curves obtained from the experimental tests a polynomial function was fitted to the force curve data for section **A**-**B,** as shown in Fig. 4b.

**4.2 Comparison of model predictions with experimental results for the glass substrate**
Figures 5 and 6 show experimental results together with model predictions for the three fluid media for the case of the glass substrate. It is noted that experimental results were not obtained for the high viscosity fluid, glycerol, at velocities exceeding 13.1 µm/s as the bending of the cantilever at these velocities was such that the laser beam deflection of the AFM fell outside the useful measuring range of the quadrant cell detector (QCD).

In Figure 5, plots corresponding to the water experiments and simulations were inserted to see in more detail the results for this fluid.

Figures 5a, 5b and 5c are plots of drag force versus tip velocity for tip-surface separations of 600, 300 and 0 nm, respectively. It can be seen in Fig. 5 that the shape of the plots is very similar in nature for the three tip-surface separations shown. In terms of the experimental results, it can be seen that, as expected, the drag force increases with the increase of velocity. In addition, the relationship between drag force and tip velocity is approximately linear in nature. This finding is in agreement with those of the investigation undertaken by Janovjak et al [13] and is further validated by the predictions from the numerical model (Fig. 5). The influence of the fluid viscosity on drag force is also readily discernible from the plots; for a given velocity, drag force increases with fluid viscosity. The average error between the numerical predictions and the experimental results shown in Fig. 5 is 15%. The largest difference between predicted drag force and experimental results tend to occur at the higher tip velocities in the fluids of greater viscosity and this may be explained by the fact that the linear relationship between the QCD response to laser position is only valid up to a certain deviation from the center of the QCD and that the Hooke's Law, used to determine the force from the deflection of the cantilever, is only applicable for small deflections.

**a) Glass substrate: drag force versus velocity for tip-surface separation of 600 nm**

**b) Glass substrate: drag force versus velocity for tip-surface separation of 300 nm**

**c) Glass substrate: drag force versus velocity for tip-surface separation of 0 nm**
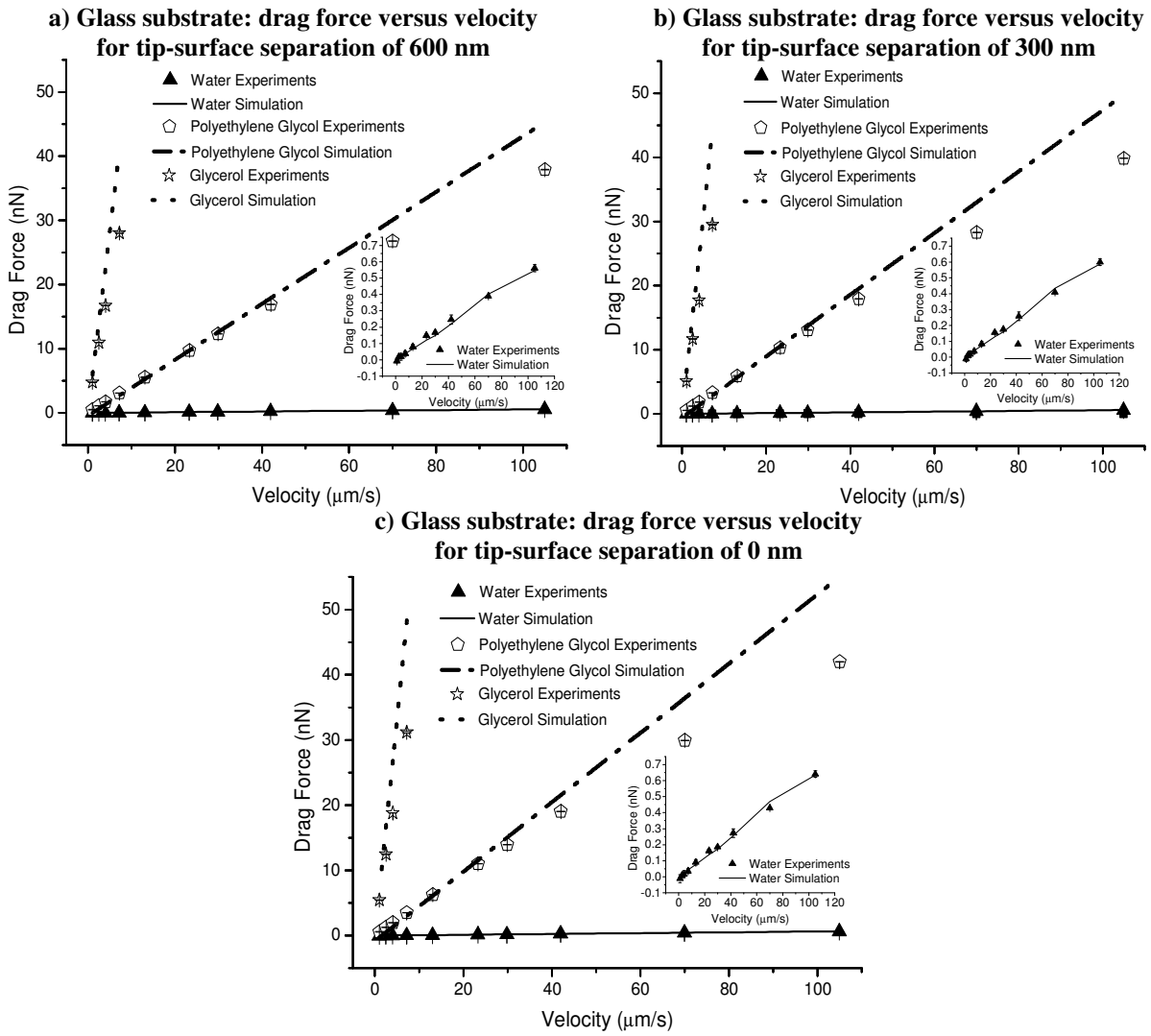
Figure 5. Glass substrate: drag force versus velocity for tip-surface separation of a) 600 nm; b) 300 nm, c) 0 nm.

The average standard deviation (SD) for the experimental drag force data shown in Fig. 5 is ± 0.05 nN.

Figures 6a, 6b and 6c are plots of drag force versus tip-surface separation for velocities of 1.05, 13.1 and 105 µm/s, respectively. It can be seen from these figures that the shape of the plots is similar in nature for the three tip velocities considered. It can be seen in Fig. 6 that an increase in drag force occurred as the cantilever tip approaches the surface. This is particularly discernible in the higher viscosity fluid media (polyethylene glycol and glycerol) and is in accordance with the findings of other researchers [20, 28].

This increase in drag force at small tip-sample separations is also predicted by the numerical model. Once again, the influence of the fluid viscosity on drag force can be readily observed. The average error between the numerical predictions and the mean experimental results shown in Fig. 6 is 15%. The average standard deviations (SD) for the experimental data shown in Fig. 6 are ± 0.036 nN, ± 0.014 nN and ± 0.14 nN for the polyethylene glycol, water and glycerol media, respectively. The average SD was calculated using 31 points along each analyzed curve.

## 4.3 Comparison of results for glass, mica and metallic substrates

Figures 7a and 7b shows drag force versus tip velocity for polyethylene fluid on the glass, mica and metallic (stainless steel) substrates, respectively, for a tip-surface separation of 300 nm and a velocity of 13.1 µm/s. The experimental results shown in Fig. 7 indicate that while the results from the three substrates are similar, drag forces are generally greater for the glass substrate than for the mica and metallic substrates.

In addition, drag forces are generally lower on the metallic substrate than on the mica substrate.

The numerical predictions for the three substrates are however identical, which indicates that additional forces not accounted for by the numerical model may be playing a role in the experimental results. These additional forces are relatively small in magnitude, and further investigation may reveal their source and enable the numerical model to be modified in order to take into account these forces.

**a) Glass substrate: drag force versus tip-surface separation for velocity of 1.05 µm/s**
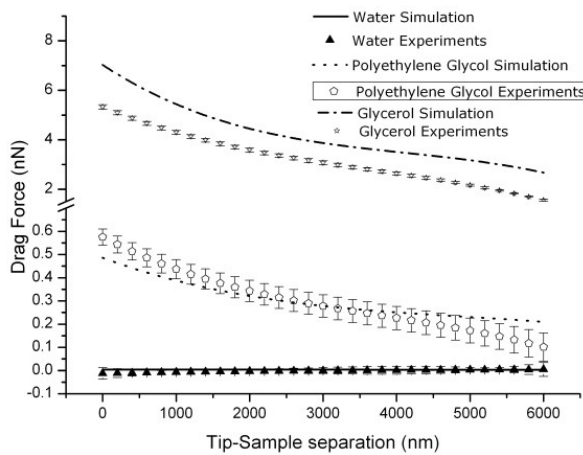
**b) Glass substrate: drag force versus tip-surface separation for velocity of 13.1 µm/s**
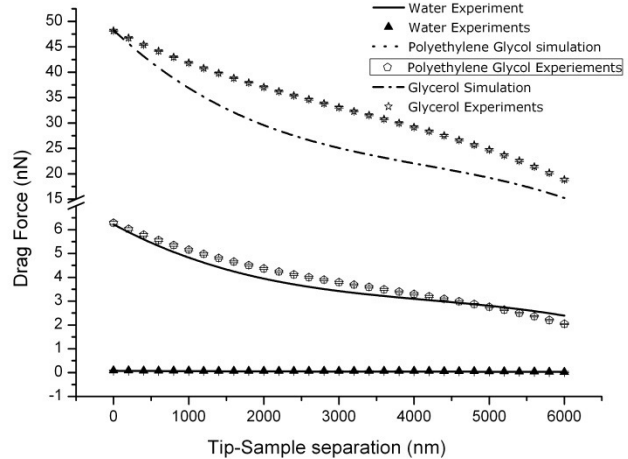
**c) Glass substrate: drag force versus tip-surface separation for velocity of 105 µm/s**
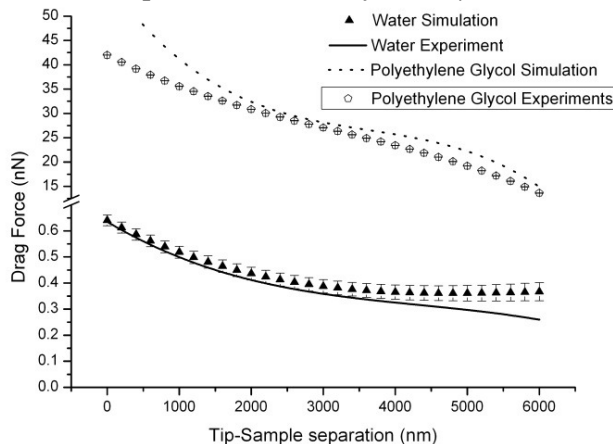


Figure 6. Glass substrate: drag force versus tip-surface separation for velocity of a) 1.05 µm/s, b) 13.1 µm/s and c) 105 µm/s.

**a) Drag force versus tip velocity for polyethylene fluid on glass, mica and metallic substrates for tip-surface separation of 300 nm**
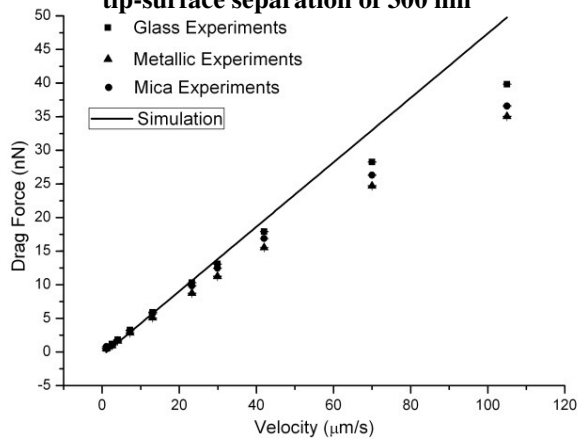
**b) Drag force versus tip velocity for polyethylene fluid on glass, mica and metallic substrates for a velocity of 13.1 μm/s.**
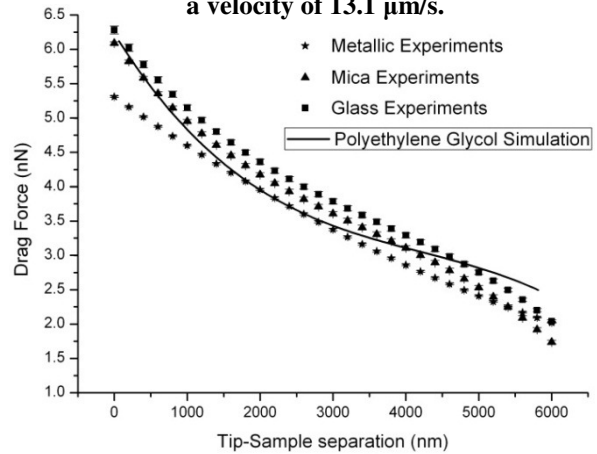
Figure 7. Drag force versus tip velocity for polyethylene fluid on glass, mica and metallic substrates a) for tip-surface separation of 300 nm and b) for a velocity of 13.1 μm/s.

## 4.4 Comparison of numerical predictions with empirical model of Janovjak et al. [13]

Alcaraz et al. [4] extended the spherical model of Brenner [18] and Cox and Brenner [19] to AFM cantilever geometries by scaling the dimension of the body and the distance to the substrate. In the model of Alcaraz et al. [4], the hydrodynamic behavior of the AFM cantilever is modeled as a drag factor, dependent on distance from the substrate. Two empirical coefficients are used, one to represent the effective cantilever tip height and the other the effective radius of the cantilever. The drag force at contact is estimated by first measuring the drag factor $b(h)$ at different tip-surface separations and then extrapolating the data to obtain a value for $h = 0$. It should be noted that the model is only valid for measurements taken near the sample (at nanometric distance) as it predicts a drag force of zero for larger separations. Janovjak et al. [13] quantified hydrodynamic drag force as a function of pulling speed and tip-sample separation for two V-shaped AFM cantilevers using the scaled spherical model of Alcaraz et al. [4].

Numerical predictions were compared against the results obtained by Janovjak et al. [13] for a small OTR4 Olympus V-shaped cantilever, as shown in Figure 8 (nominal dimensions: stiffness 0.095 N/m, length 100 μm, width 18 μm, thickness 0.4 μm) in water. It is noted that it was not possible to provide predictions for comparison purposes for the second case of the larger V-shaped cantilever in phosphate buffered saline (PBS) medium as accurate PBS fluid properties could not be confirmed.

To compare the results of Janovjak with the coupled model developed in the work presented herein, the methodology described previously (Section 3.2) to calculate an effective Young's modulus for the OTR4 Olympus cantilever was used (Figure 8). The value of the effective Young's modulus calculated for this cantilever was 186.1 GPa.

The comparison between numerical predictions and the analytical model is shown in Fig. 9. Figure 9a is a plot of drag force versus tip velocity for the small V-shaped cantilever. From this figure, it can be seen that the predictions from the numerical model are in good agreement with the empirical model.

12

**Dimensions of cantilever model OTR4 Olympus
with 0.4 μm thickness**
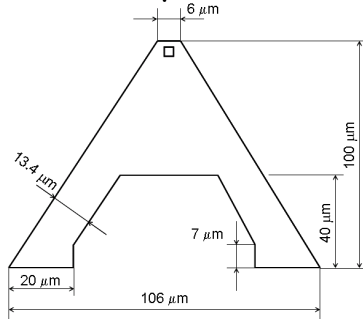


Figure 8 Cantilever model OTR4 Olympus with 0.4 μm thickness.

The linear dependence of drag force on tip velocity can be clearly seen. This result confirms the relationship between drag force and tip velocity established from the results of the experimental tests described in this paper. Figure 9b is a plot of drag force versus tip-sample separation for the small V-shaped cantilever. Again, a good agreement is obtained between the two models. The more complex dependence of drag force on tip-sample separation is evident, with an increase in drag force close to the surface being experienced. This increase was clearly visible in the results of the experimental tests presented previously in this paper. The average errors between the predictions from the numerical model and the empirical model are 2% and 8% for Fig. 9a and Fig. 9b, respectively.
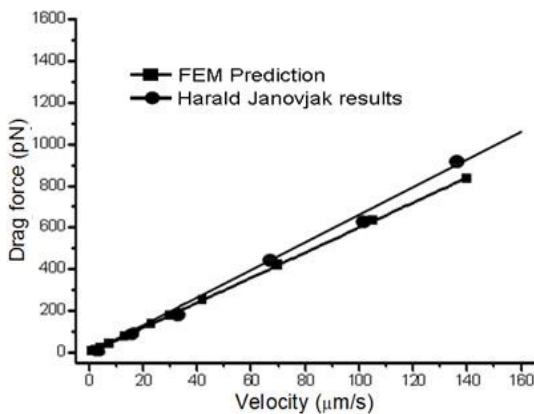
## 4.5 Drag force simulation including cell geometry

The model utilized in the previous section to calculate hydrodynamic drag force does not consider the possible influence of the presence of a biological cell on the hydrodynamic drag forces generated. To investigate drag forces when a cell is included, a simplified cell geometry shown in Fig. 10a with dimensions detailed in Fig. 10b was incorporated in the model. In practice, the exact cell geometry is difficult to obtain and it varies enormously from cell to cell, however, the use of the approximate cell geometry shown in Fig. 10b was considered adequate for this investigation.

The cantilever tip is initially at a distance of 6000 nm above the platform and a cantilever tip velocity of 30 µm/s is employed. The total distance travelled in this simulation is 4000 nm.

To incorporate the cell into the model, the cell volume was subtracted from the original fluid model, leaving a well having the geometry of the cell (Fig. 10c). The boundary condition applied to the fluid surfaces in contact with the cell is the same as that applied to the 'base' surface, i.e. a no-slip boundary condition is applied.

a) Comparison of numerical predictions with results from Janovjak et al. [13] using empirical model of Alcaraz et al. [4]: drag force versus tip velocity for tip-sample separation of 500 nm

b) Comparison of numerical predictions with results from Janovjak et al. [13] using empirical model of Alcaraz et al. [4]: drag force versus tip-sample separation for tip velocity of 70 µm/s.
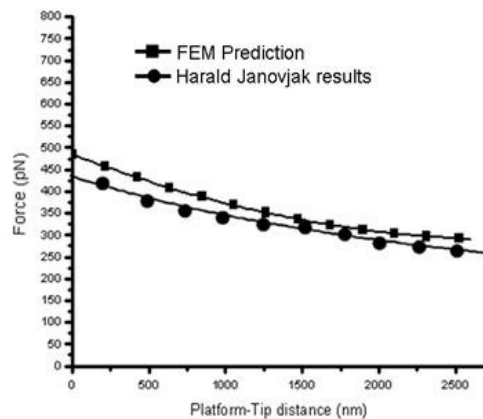


Figure 9. Comparison of numerical predictions with results from Janovjak et al. [13] using empirical model of Alcaraz et al. [4]: a) drag force versus tip velocity for tip-sample separation of 500 nm; b) drag force versus tip-sample separation for tip velocity of 70 µm/s.

13

**a) 3D model of a cell**

**b) Cell dimensions**

**c) Cantilever tip and cell model**
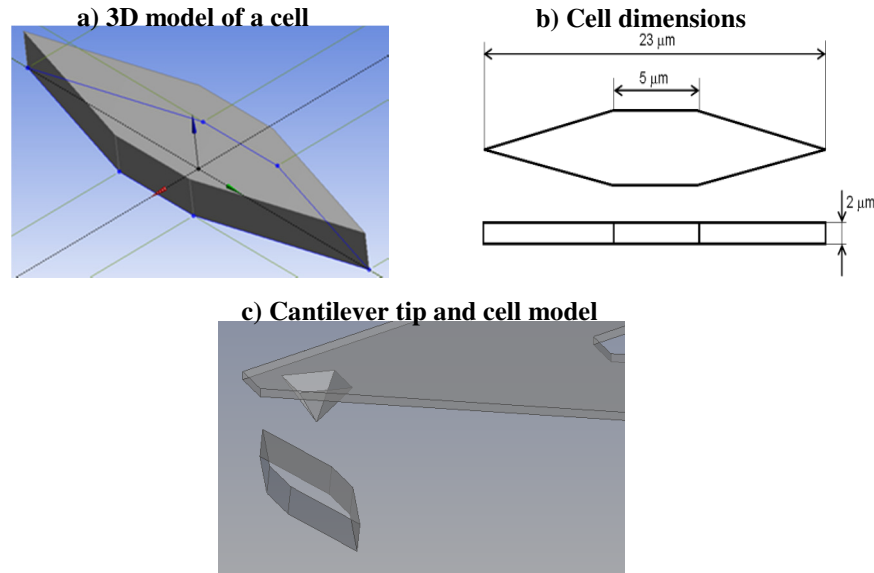
Figure 10. a) 3D cell model, b) cell dimensions, c) Cantilever tip and cell model

Figure 11 shows the results of the investigation undertaken with and without the cell being included in the model. It can be seen upon inspection of this figure that the drag forces obtained in the model when the cell geometry was included are of bigger magnitude than the drag forces obtained in the model when the cell was not included; the difference in the results was being approximately 16.5%. This change in the drag forces is attributed to the fact that the cell volume modifies the water flow when the cantilever tip approaches the cell.

Based in this example, it can be seen that the finite element method is an important and useful tool for predicting the drag force in AFM measurements. This technique has a number of advantages compared with empirical and analytical models, namely it is not necessary to determine empirical or geometrical factors before applying the model. In addition, the model can be easily modified for different cantilever geometries, materials and for different fluid media.

## 5. Conclusions

A numerical integrated model that is able to provide accurate predictions of drag force present in AFM measurements in fluids, over a wide range of cantilever tip velocities, tip-sample separations and fluid viscosities, was presented.



Figure 11. Drag forces in the model with and without a cell in water simulations.

One of the major advantages of the numerical model is that only one experimental test is required to determine the model parameters for simulations.

Numerical results were compared with extensive experimental data and analytical predictions and good agreement was observed. An average error of 15% was observed between model predictions and the experimental results undertaken using the glass substrate. An average error of 2% was calculated between the numerical results and the analytical model predictions for the

14

influence of tip velocity on drag force results; the average error was 8% for the results of the influence of tip-sample separation on drag force.

The findings in this paper confirmed that drag force dependence on tip speed is essentially linear in nature. The numerical model developed in this work was capable of predicting the increase in drag force at distances close to the sample observed experimentally. In addition, the model can be employed over the range of tip geometries and velocities typically utilized in AFM measurements.

It is expected that the model will enable increased accuracy of AFM studies of biological samples in fluids, where in vivo measurements are important, without the need for extrapolation of experimental data.

## References

[1] H.-J. Butt, B. Cappella, M. Kappl, Force measurements with the atomic force microscope: Technique, interpretation and applications, Surf. Sci. Rep. 59 (2005) 1-152.

[2] A.L. Weisenhorn, M. Khorsandi, S. Kasas, V. Gotzos, H.J. Butt, Deformation and height anomaly of soft surfaces studied with an AFM, Nanotechnol. 4 (1993) 106-113.

[3] P. Maivald, H.J. Butt, S.A.C. Gould, C.B. Prater, B. Drake, J.A. Gurley, V.B. Elings, P.K. Hansma, Using force modulation to image surface elasticities with the atomic force microscope, Nanotechnol. 2 (1991) 103-106.

[4] J. Alcaraz, L. Buscemi, M. Puig-de-Morales, J. Colchero, A. Baró, D. Navajas, Correction of Microrheological Measurements of Soft Samples with Atomic Force Microscopy for the Hydrodynamic Drag on the Cantilever, Langmuir 18 (2002) 716-721.

[5] Y.M. Efremov, E.A. Pukhlyakova, D.V. Bagrov, K.V. Shaitan, Atomic force microscopy of living and fixed Xenopus laevis embryos, Micron 42 (2011) 840-852.

[6] A. Ortega-Esteban, I. Horcas, M. Hernando-Pérez, P. Ares, A.J. Pérez-Berná, C. San Martín, J.L. Carrascosa, P.J. de Pablo, J. Gómez-Herrero, Minimizing tip–sample forces in jumping mode atomic force microscopy in liquid, Ultramicroscopy 114 (2012) 56-61.

[7] A. Vinckier, G. Semenza, Measuring elasticity of biological materials by atomic force microscopy, FEBS Lett. 430 (1998) 12-16.

[8] B. Drake, C. Prater, A. Weisenhorn, S. Gould, T. Albrecht, C. Quate, D. Cannell, H. Hansma, P. Hansma, Imaging crystals, polymers, and processes in water with the atomic force microscope, Science 243 (1989) 1586-1589.

[9] A. Engel, D.J. Muller, Observing single biomolecules at work with the atomic force microscope, Nat. Struct. Mol. Biol. 7 (2000) 715-718.

[10] D.J. Muller, J. Helenius, D. Alsteens, Y.F. Dufrene, Force probing surfaces of living cells to molecular resolution, Nat. Chem. Biol. 5 (2009) 383-390.

[11] M. Radmacher, R. Tillamnn, M. Fritz, H. Gaub, From molecules to cells: imaging soft samples with the atomic force microscope, Science 257 (1992) 1900-1905.

[12] M.B. Viani, L.I. Pietrasanta, J.B. Thompson, A. Chand, I.C. Gebeshuber, J.H. Kindt, M. Richter, H.G. Hansma, P.K. Hansma, Probing protein-protein interactions in real time, Nat. Struct. Mol. Biol. 7 (2000) 644-647.

[13] H. Janovjak, J. Struckmeier, D.J. Müller, Hydrodynamic effects in fast AFM single-molecule force measurements, Eur. Biophys. J. 34 (2005) 91-96.

[14] R. Liu, M. Roman, G. Yang, Correction of the viscous drag induced errors in macromolecular manipulation experiments using atomic force microscope, Rev. Sci. Instrum. 81 (2010) 063703-1-063703-5.

[15] K. Sarangapani, H. Torun, O. Finkler, C. Zhu, L. Degertekin, Membrane-based actuation for high-speed single molecule force spectroscopy studies using AFM, Eur. Biophys. J. 39 (2010) 1219-1227.

[16] A. Farokh Payam, Sensitivity of flexural vibration mode of the rectangular atomic force microscope micro cantilevers in liquid to the surface stiffness variations, Ultramicroscopy 135 (2013) 84-88.

[17] A. Raman, J. Melcher, R. Tung, Cantilever dynamics in atomic force microscopy, Nano Today 3 (2008) 20-27.

[18] H. Brenner, The slow motion of a sphere through a viscous fluid towards a plane surface, Chem. Eng. Sci. 16 (1961) 242-251.

[19] R.G. Cox, H. Brenner, The slow motion of a sphere through a viscous fluid towards a plane surface—II Small gap widths, including inertial effects, Chem. Eng. Sci. 22 (1967) 1753-1777.

[20] H. Ma, J. Jimenez, R. Rajagopalan, Brownian Fluctuation Spectroscopy Using Atomic Force Microscopes, Langmuir 16 (2000) 2254-2261.

[21] R.E. Mahaffy, C.K. Shih, F.C. MacKintosh, J. Käs, Scanning Probe-Based Frequency-Dependent Microrheology of Polymer Gels and Biological Cells, Phys. Rev. Lett. 85 (2000) 880-883.

[22] C. Nemes, N. Rozlosnik, J.J. Ramsden, Direct measurement of the viscoelasticity of adsorbed protein layers using atomic force microscopy, Phys. Rev. E 60 (1999) R1166-R1169.

[23] M. Radmacher, M. Fritz, C.M. Kacher, J.P. Cleveland, P.K. Hansma, Measuring the viscoelastic properties of human platelets with the atomic force microscope, Biophys. J. 70 (1996) 556-567.

[24] J.L. Hutter, J. Bechhoefer, Calibration of atomic-force microscope tips, Rev. Sci. Instrum. 64 (1993) 1868-1873.

[25] H. Bonakdari, A.A. Zinatizadeh, Influence of position and type of Doppler flow meters on flow-rate measurement in sewers using computational fluid dynamic, Flow Meas. Instrum. 22 (2011) 225-234.

[26] J. te Riet, A.J. Katan, C. Rankl, S.W. Stahl, A.M. van Buul, I.Y. Phang, A. Gomez-Casado, P. Schön, J.W. Gerritsen, A. Cambi, A.E. Rowan, G.J. Vancso, P. Jonkheijm, J. Huskens, T.H. Oosterkamp, H. Gaub, P. Hinterdorfer, C.G. Figdor, S. Speller, Interlaboratory round robin on cantilever calibration for AFM force spectroscopy, Ultramicroscopy 111 (2011) 1659-1669.

[27] J.E. Sader, Parallel beam approximation for V-shaped atomic force microscope cantilevers, Rev. Sci. Instrum. 66 (1995) 4583-4587.

[28] A. Roters, D. Johannsmann, Distance-dependent noise measurements in scanning force microscopy, J. Phys. Condens. Matter 8 (1996) 7561–7577.